

# Bulk and Interfacial Effects in the Co/Ni<sub>x</sub>Mn<sub>100-x</sub> Exchange-Bias System due to Creation of Defects by Ar<sup>+</sup> Sputtering

Tauqir Shinwari, Ismet Gelen, Yasser A. Shokr, Ivar Kumberg, Ikramullah, Muhammad Sajjad, Wolfgang Kuch,\* and M. Yaqoob Khan\*

A series of experiments is carried out to identify the contribution of interface and bulk antiferromagnetic (AFM) spins to exchange bias (EB) in ultrathin epitaxial ferromagnetic (FM)/AFM bilayer samples. These are single-crystalline AFM Ni<sub>x</sub>Mn<sub>100-x</sub> and ferromagnetic Co layers on Cu<sub>3</sub>Au(001), deposited under ultrahigh vacuum conditions, in which structural or chemical defects are deliberately introduced by controlled Ar ion sputtering at the surface of the AFM layer or at a certain depth inside the AFM layer. Comparison of the magnetic properties measured by magneto-optical Kerr effect for sputtered and non-sputtered parts of the same sample then allows a precise determination of the influence of sputtering on the AFM layer during the sample preparation, whereas all other parameters are kept identical. The results show that the creation of defects in the bulk of the AFM layer enhances the magnitude of EB and its blocking temperature, but not the creation of defects at the interface. It is also observed that the deeper the insertion of defects in the AFM layer, the higher the value of the EB field and the larger the coercivity. These findings are discussed as the effect of additional pinning centers in the bulk of the AFM layer.

## 1. Introduction

Research on ultrathin magnetic layers and layered materials has reached an enormous impact, both scientifically and economically, with respect to applications in magnetic data storage technology, as sensors, or for future electronics utilizing the spin rather than the charge of electrons, the so-called “spintronics”.<sup>[1-4]</sup> The physical size of a bit of information in magnetic data storage is already in the nanometer regime and is still shrinking, following the ever-increasing demand for higher recording densities. Very soon the dimension of the recording bit will reach the sub-10 nm range. This poses formidable challenges to the read sensors. One ingredient of hard disk read sensors are magnetic layered systems in which ferromagnetic (FM) and antiferromagnetic (AFM) materials are in contact.<sup>[5]</sup> They show the exchange bias (EB) effect, which has received increased


attention during the past decades.<sup>[6-11]</sup> It manifests itself in a shift of the magnetic hysteresis loop of the FM layer along the field axis.<sup>[12]</sup> Although reported first in 1956,<sup>[13]</sup> it was only in the mid-1990s that it shifted into the center of interest, triggered by applications of FM/AFM heterostructures for tailoring the magnetic properties of magnetoresistive devices. The past years have seen significant advances toward an explanation of the effect, however, a fundamental microscopic picture of the origin of the unidirectional magnetic anisotropy present in the EB effect is still missing.

The occurrence of EB requires two basic ingredients: a magnetic interaction between FM and AFM spins at the interface, and a pinning of magnetic moments against the reversal of the FM-layer magnetization by the external magnetic field inside the AFM layer. As in AFM materials the direction of the spins varies on the length scale of single atomic distances, a thorough characterization of the atomic structure of the films and their interface is mandatory for fundamental investigations into the effect. In the commonly used polycrystalline systems prepared by sputtering techniques this is naturally not the case. A promising approach is the investigation of single-crystalline systems.<sup>[14-19]</sup> In such systems, it is shown, for example, that the magnetic coupling between AFM and FM layers is due to

T. Shinwari, I. Gelen, Dr. Y. A. Shokr, I. Kumberg, Prof. W. Kuch  
Institut für Experimentalphysik  
Freie Universität Berlin  
Arnimallee 14, Berlin 14195, Germany  
E-mail: kuch@physik.fu-berlin.de

Dr. Ikramullah, Dr. M. Sajjad, Dr. M. Y. Khan  
Department of Physics  
Kohat University of Science and Technology  
Kohat, Khyber Pakhtunkhwa 26000, Pakistan  
E-mail: yaqoob@kust.edu.pk

Dr. Y. A. Shokr  
Faculty of Science, Department of Physics  
Helwan University  
Cairo 17119, Egypt

 The ORCID identification number(s) for the author(s) of this article can be found under <https://doi.org/10.1002/pssr.202100195>.

© 2021 The Authors. physica status solidi (RRL) Rapid Research Letters published by Wiley-VCH GmbH. This is an open access article under the terms of the Creative Commons Attribution-NonCommercial License, which permits use, distribution and reproduction in any medium, provided the original work is properly cited and is not used for commercial purposes.

DOI: 10.1002/pssr.202100195

single-atomic steps at the interface, whereas atomically flat terraces hardly contribute.<sup>[19]</sup> Single-crystalline films of AFM binary alloys such as FeMn or NiMn can be grown by codeposition of the constituents on single-crystalline substrates in ultrahigh vacuum.<sup>[5,17,19,20]</sup> Such films often exhibit a noncollinear AFM spin structure,<sup>[14,21]</sup> which can couple magnetically to FM layers with both either an in-plane or an out-of-plane easy axis of magnetization.<sup>[14,22]</sup>

The technological importance of EB and exciting physics triggered extensive research to uncover its complicated and sensitive nature. Originally, the EB effect was considered an interfacial phenomenon, backed by some models.<sup>[23–28]</sup> Later work revealed that the EB is not simply interfacial, but there is some contribution from the bulk of the AFM, too. This issue was first addressed in the domain-state model.<sup>[6,7,29]</sup> It describes EB in terms of uncompensated pinning moments present within the bulk of the AFM. In the past few years, different systems were explored experimentally and evidence was always favoring the idea that the bulk spin structure of an AFM plays an important role in deciding the EB effect.<sup>[11,30–34]</sup> These reports proposed that the bulk AFM incorporates uncompensated moments to hold or pin the neighboring FM layers in one direction. Recently, Khan et al.<sup>[33]</sup> reported the contribution of the bulk spin structure in single-crystalline Ni/NiMn/Ni trilayers. They explained their data by a model of competing noncollinear pinning centers throughout the AFM Ni<sub>25</sub>Mn<sub>75</sub> layer, which couple to the adjacent FM layers via coupling paths leading all the way to the interface.

Here, we investigate the role of controlled structural defects in an epitaxial bilayer system for the EB. To do so, one needs a system with a relatively low number of intrinsic defects, i.e., epitaxial single-crystalline films. By deliberately creating a certain number of defects, their effect on the resulting EB field can be studied. We introduce defects by a short bombardment with Ar ions at moderate energies at different depths inside the AFM layer or at the very top of the AFM layer, at the interface to the FM layer. By exposing only half of the sample to the ion bombardment, all other deposition parameters like alloy composition, thickness, growth rate, or substrate temperature, small variations of which could have already a measurable influence on the resulting EB field and the coercivity, are strictly the same. Comparison of the magnetic properties measured at the two parts of the sample then allows a precise determination of the influence of the additional step during the sample preparation. We chose Co/Ni<sub>x</sub>Mn<sub>100–x</sub> bilayers on Cu<sub>3</sub>Au(001) for our investigation, since it is a well-explored single-crystalline EB system. A benefit of using single-crystalline instead of polycrystalline samples is to better control the film structural properties, in particular also at the interfaces. While face-centered tetragonal (FCT) NiMn grows along the *a* axis on a Cu(001) single crystal surface,<sup>[20,35]</sup> on Cu<sub>3</sub>Au(001) it grows like its bulk counterpart along the *c* axis.<sup>[17,22]</sup> Ni<sub>x</sub>Mn<sub>100–x</sub> exhibits layer-by-layer growth on Cu<sub>3</sub>Au(001) as demonstrated by oscillations of the specularly reflected intensity of medium-energy electron diffraction (MEED) shown in Figure 1. We focus on epitaxially grown bilayers Co/Ni<sub>x</sub>Mn<sub>100–x</sub>/Cu<sub>3</sub>Au(001) including pure Mn using the magneto-optical Kerr effect (MOKE) to detect the EB effect. NiMn film thicknesses of around 30 atomic monolayers (ML) are preferred because they display a reasonable EB shift. The growth

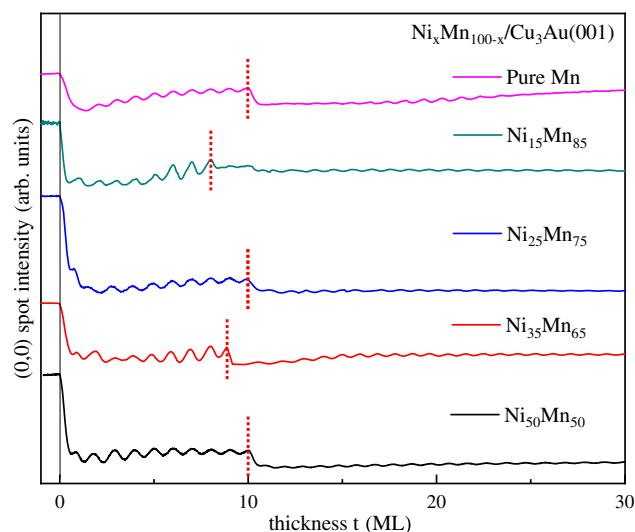


**Figure 1.** MEED curves of the (0,0) spot recorded during the deposition of Ni<sub>x</sub>Mn<sub>100–x</sub> films on Cu<sub>3</sub>Au(001) at 300 K for various values of *x*. The shutter was opened at 0 ML and closed at the dashed vertical bars, then after creating defects it was opened at the very same bars and closed at the end, i.e., at 30 ML.

of these systems has already been studied and is well-controlled.<sup>[16,17,21,22,36–38]</sup> They exhibit EB above a certain AFM layer thickness. Co is used as FM layer, which grows epitaxially on Cu<sub>3</sub>Au(001) as well as on top of the NiMn or Mn AFM layers,<sup>[16,17,21,22,38]</sup> and exhibits an in-plane easy axis of magnetization. Our results show that the controlled insertion of disorder at the interface or at defined depths of the AFM layer provides uncompensated pinned moments, resulting in an increase in the EB effect and an enhanced blocking temperature. A stronger effect is observed for deeper depths of the inserted defects.

## 2. Results

We first present investigations of the growth of the single-crystalline bilayers and the effect of the Ar ion bombardment. The growth of AFM Ni<sub>x</sub>Mn<sub>100–x</sub> on Cu<sub>3</sub>Au(001) at *T* = 300 K was monitored by means of MEED for the concentration range from pure Mn to equiatomic NiMn. Figure 1 shows the reflected MEED intensity as a function of deposition time for increasing Ni content *x* from top to bottom. The curves are normalized to the initial MEED intensity at the time before opening the shutters of the evaporators, i.e., at *t* = 0, and shifted vertically for clarity. The deposition time was converted into a monolayer thickness scale under the assumption that a maximum in the MEED intensity corresponds to a filled integer monolayer, neglecting a possible phase shift. This conversion allows a convenient presentation of MEED curves obtained from films deposited at different growth rates in a single figure. An oscillating MEED intensity, which is a fingerprint of a layer-by-layer growth mode, was found for all Ni<sub>x</sub>Mn<sub>100–x</sub> films. The MEED oscillations of the NiMn alloy on Cu<sub>3</sub>Au(001) exhibit improved layer-by-layer growth in comparison with NiMn on Cu(001), which only shows 15 pronounced maxima.<sup>[20]</sup> The reason may

lie in the differences in lattice mismatch with the different substrates. NiMn has less mismatch with  $\text{Cu}_3\text{Au}(001)$  in comparison with the  $\text{Cu}(001)$  substrate. The growth axis of the NiMn alloy on both substrates is also different.<sup>[16,20,22,35]</sup> At the thicknesses indicated by the vertical bars, the Ar sputtering was applied. The effect on the layer-by-layer growth is clearly visible. The reduction in the amplitude of oscillation indicates the onset of a more simultaneous growth of several layers.

**Figure 2** shows LEED patterns of  $\text{Ni}_x\text{Mn}_{100-x}$  films on  $\text{Cu}_3\text{Au}(001)$  at 300 K. As the main purpose of this study is the comparison of the magnetic properties of the sputtered and non-sputtered parts of the same sample, it is important to show that the crystalline structure on both parts of the sample is very similar. LEED was performed directly after sputtering one part of the sample. The only difference which we want to show here is that while producing controlled defects in one part of the sample, there is a slight change in the intensity of the LEED spots, as is observable from **Figure 2** and is further supported by **Figure 3**, presenting line scans across the two  $\langle 11 \rangle$  and one  $\langle 10 \rangle$  spot for different samples. Consistent peak positions indicate coherent growth throughout at least a thickness of  $\approx 10$  ML. The non-sputtered part of the  $\text{Ni}_x\text{Mn}_{100-x}$  films exhibits sharp LEED spots and a high ratio of peak intensity to background. In contrast, the sputtered part of the  $\text{Ni}_x\text{Mn}_{100-x}$  films exhibits a bit dimmer spots in which the peak intensity decreases. This suggests that after producing defects the surface becomes a bit

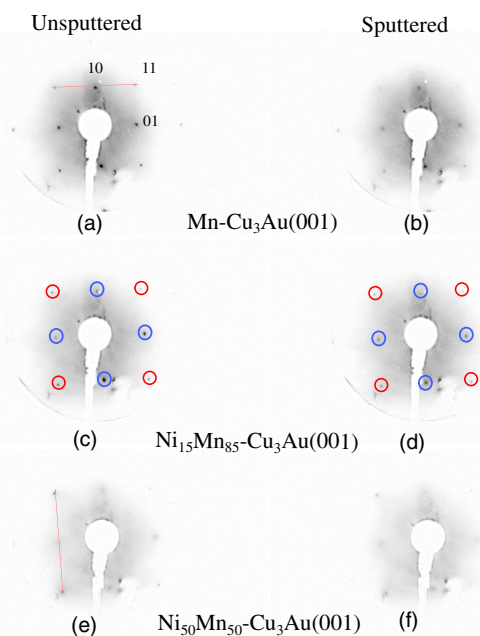


**Figure 2.** a–e) LEED patterns of  $\approx 10$  monolayers thick  $\text{Ni}_x\text{Mn}_{100-x}$  films grown on  $\text{Cu}_3\text{Au}(001)$  at  $T = 300$  K: non-sputtered and sputtered Mn (a,b),  $\text{Ni}_{15}\text{Mn}_{85}$  (c,d), and  $\text{Ni}_{50}\text{Mn}_{50}$  (e,f). The integer spot positions are highlighted in (c) and (d). The patterns show  $c(2 \times 2)$  structure, not to be confused with artifacts of the used LEED system close to the rim of the electron gun. (a) and (e) show how the line profiles are obtained using a line on three spots, in the same way for both the sputtered and non-sputtered part of the samples. Crystallographic labels are indicated in (a).

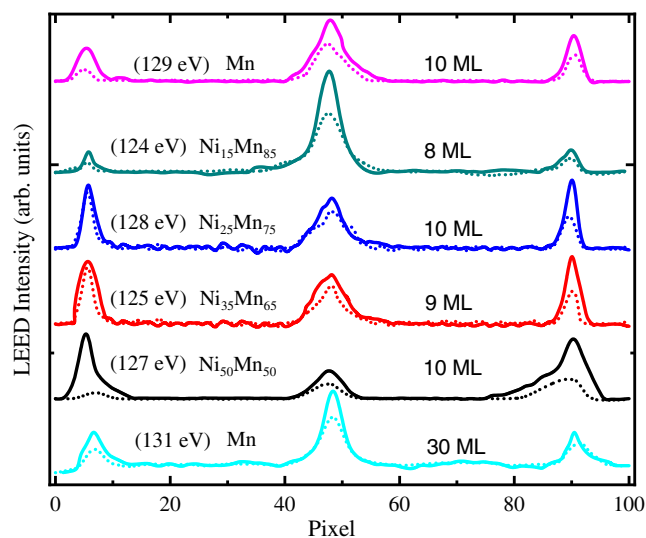


**Figure 3.** Intensity profiles (line scans) measured across LEED patterns for  $\text{Ni}_x\text{Mn}_{100-x}$  films on  $\text{Cu}_3\text{Au}(001)$ . The dotted and straight lines for each sample show the comparison of the sputtered and the non-sputtered parts of the same samples, respectively. The electron energy (mentioned at the left side of each line scan) is the same for the two parts of the same sample and nearly equal for all samples.

rougher, which results in less intensity of the LEED spots as compared with the non-sputtered part.

**Figure 4** shows STM images pristine  $\text{Cu}_3\text{Au}(001)$  (**Figure 4a**), non-sputtered 4 ML  $\text{Mn}/\text{Cu}_3\text{Au}(001)$  (**Figure 4c**), and sputtered 4 ML  $\text{Mn}/\text{Cu}_3\text{Au}(001)$  films (**Figure 4e**). **Figure 4b,d,f** show line profiles taken along the solid lines in images **Figure 4a,c,e**, respectively. **Figure 4c,e**, shows Mn films with atomically flat surfaces with small 2D islands of single atomic height on top, which have feature sizes of several nanometers. This observation is consistent with the layer-by-layer growth concluded from the MEED oscillations. Furthermore, a clear well-ordered surface is observed for the non-sputtered 4 ML Mn film, whereas a somewhat enhanced roughness can be seen on the surface of sputtered 4 ML  $\text{Mn}/\text{Cu}_3\text{Au}(001)$ . These results are in accordance with **Figure 2** and **3**. The separation between Mn atomic planes is obtained from the line scans.

We now turn to the magnetic characterization of the samples. Hysteresis loops are measured by longitudinal MOKE at different temperatures after field cooling with  $+20$  mT from above the Néel temperature ( $T_N$ ) of Mn and below the Curie temperature ( $T_C$ ) of the Co, i.e., from  $\approx 480$  K, which provided an EB shift along the negative field direction. **Figure 5** shows an example of temperature-dependent hysteresis loops. Here, the sample is 10 ML Co/30 ML Mn/ $\text{Cu}_3\text{Au}(001)$  in panel (a) and 10 ML Co/20 ML Mn/sputtered/10 ML Mn/ $\text{Cu}_3\text{Au}(001)$  in panel (b).

Nearly rectangular-shaped loops for both cases are obtained, where a coercivity ( $H_C$ ) enhancement with decreasing temperature can be observed. Although the general behavior of the temperature-dependent hysteresis loops is similar for the non-sputtered and sputtered cases, the details are different. The main differences are 1)  $H_C(T)$  for the sputtered part is almost 1.5 times that of the non-sputtered part at low temperatures, and the reduction of  $H_C$  to lower values occurs at higher temperatures

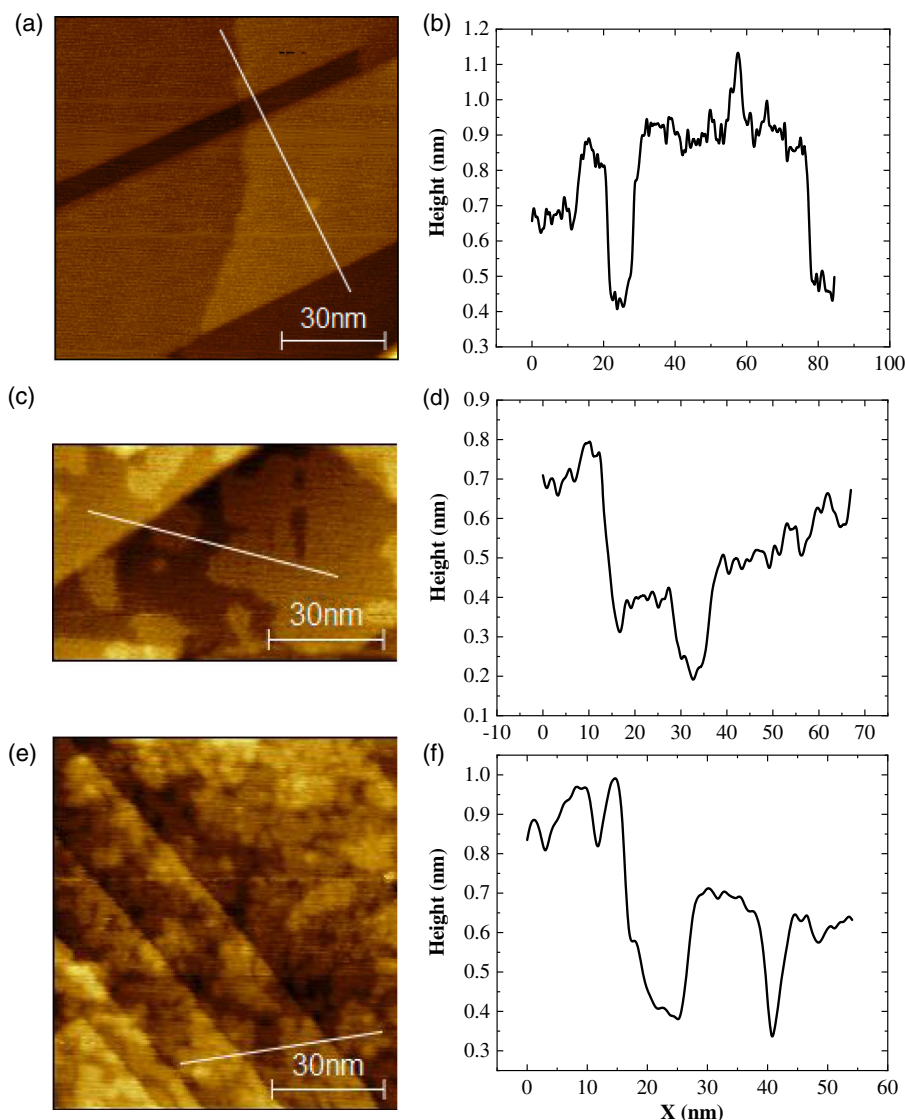


**Figure 4.** a,c,e) Constant-current STM topography images ( $U = 1\text{ V}$ ,  $I = 0.48\text{ nA}$ ): a) pristine  $\text{Cu}_3\text{Au}(001)$  substrate, c) room-temperature deposited nonsputtered, and e) sputtered 4 ML Mn on  $\text{Cu}_3\text{Au}(001)$ . b,d,f) Line profiles along the white lines in images (a,c,e), respectively.

for the sputtered part (loop at 400 K); 2) the EB field ( $H_{\text{eb}}$ ) for the sputtered part is vanishing at  $\approx 420\text{ K}$ , while it ceases for the nonsputtered part below  $\approx 260\text{ K}$ , which means that the blocking temperature is also nearly doubled. In this kind of magnetic thin film,  $H_c$  of the FM layer alone can decrease monotonically (with a small slope) with increasing temperature. A monotonic decrease in  $H_c$  could thus be present also in the absence of exchange coupling between the AFM and the FM layers. However, we observe a discontinuity in the slope of  $H_c$  versus temperature, which is typical for exchange-coupled AFM/FM bilayer systems.<sup>[18,39,40]</sup> The point at which this discontinuity of the temperature-dependent  $H_c$  occurs is considered as  $T_N$ . For its estimation, we follow the procedure already used in the study by Stampe et al.<sup>[18]</sup> and fit a straight line to the high-temperature side of the  $H_c(T)$  data to represent the behavior of the uncoupled FM layer. The temperature value below which the measured  $H_c$  significantly diverges from this line is defined as Néel

temperature  $T_N$  of the AFM layer in the bilayer. To avoid an alloying effect of the AFM and FM materials at the interface, we did not take measurements above 500 K.

**Figure 6** shows the temperature-dependent evaluation of  $H_c$  (Figure 6a) and  $H_{\text{eb}}$  (Figure 6b) for samples with different concentrations  $x$  but similar thickness of  $\approx 30\text{ ML}$  of  $\text{Ni}_x\text{Mn}_{100-x}$ , either sputtered after the deposition of  $\approx 10\text{ ML}$  or nonsputtered, in contact with in-plane magnetized Co. The main observation is that the EB and also the blocking temperature  $T_b$  are higher for the sputtered samples compared with the nonsputtered ones. The largest relative increase in  $H_{\text{eb}}$  due to sputtering is observed for  $x = 0$  and  $x = 50$ . The sputtering also increases the coercivities, but except for the pure Mn AFM layer this increase is relatively small.  $T_N$  does not change much due to sputtering. While the four Ni-containing samples exhibit increasing  $H_{\text{eb}}$  with decreasing  $x$ , the EB field is again somewhat lower when going from  $x = 15$  to  $x = 0$ . For  $H_c$ , the behavior is opposite: here the

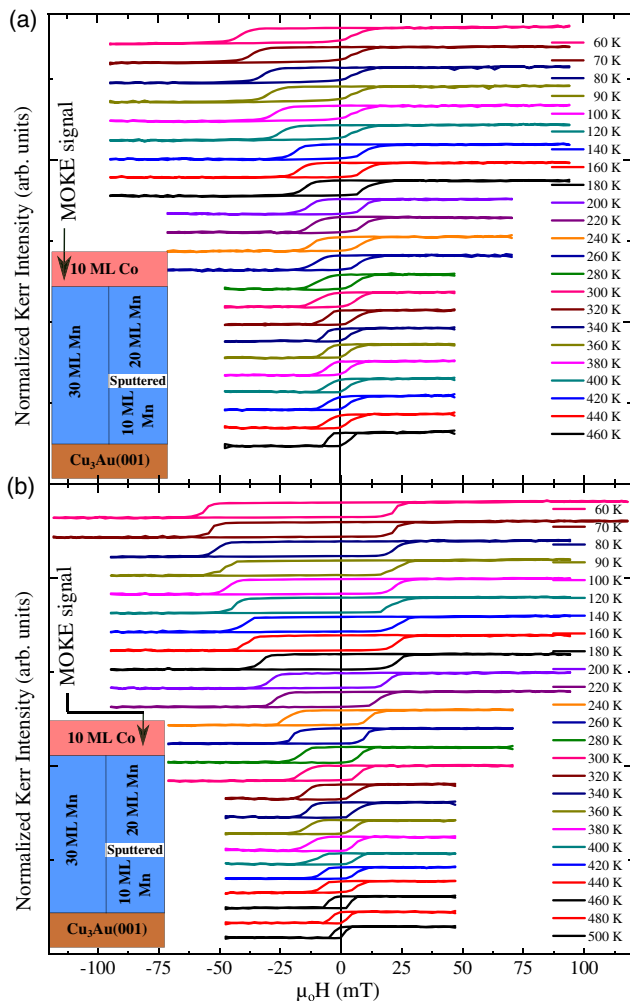


**Figure 5.** a,b) Normalized hysteresis loops for 10 ML Co/30 ML Mn/Cu<sub>3</sub>Au(001) for the non-sputtered (a) and sputtered (b) parts of the sample, measured with longitudinal MOKE at different temperatures. The sample was field-cooled in +20 mT from ≈480 K, above  $T_N$  of Mn and below the Curie temperature of the Co film. The insets (sketches) illustrate the two parts of the sample, non-sputtered and sputtered, respectively.

films with  $x = 0$  and  $x = 50$  present the highest values. Similar trends of  $H_{eb}$  and  $H_c$  with  $Ni_xMn_{100-x}$  concentration for non-sputtered samples have been presented in the studies,<sup>[16,21]</sup> for bilayers NiMn/Ni/(Co)/Cu<sub>3</sub>Au(001). The difference to the results presented here is that in these studies by Khan et al.,<sup>[16,21]</sup> 2 ML Co were deposited first on Cu<sub>3</sub>Au(001) and Ni on top of it before NiMn as an AFM layer has been deposited, whereas here we deposited NiMn directly on the Cu<sub>3</sub>Au(001) crystal, introduced some defects within or on the surface of NiMn by argon sputtering, and then placed the Co layer on top.

**Figure 7** shows  $H_c(T)$  and  $H_{eb}(T)$  for three samples with pure Mn AFM layer of equal thicknesses. Here, defects are produced at different depths in the AFM Mn layer (from bottom to surface). The non-sputtered parts of all three samples show nearly the same  $H_c(T)$ , as expected, whereas an increase is observed in the sputtered parts when we go deeper with the insertion of defects. It shows that sputtering at a larger depth is having a

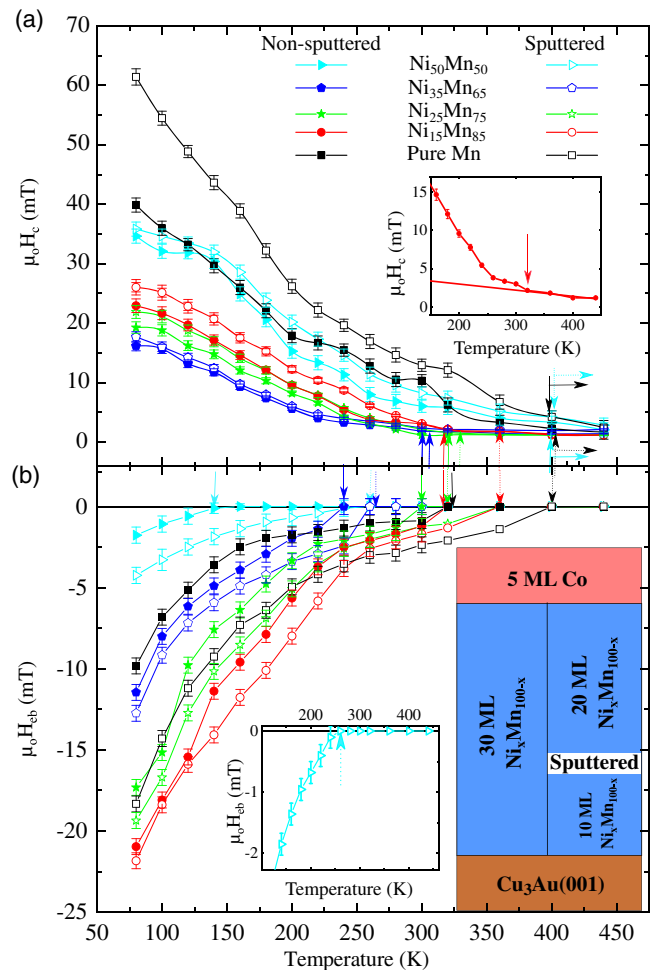


**Figure 6.** a,b) Temperature dependence of  $H_c$  (a) and  $H_{eb}$  in 5 ML Co/30 ML  $Ni_xMn_{100-x}$  bilayers on Cu<sub>3</sub>Au(001) for different Ni concentrations  $x$ . The sketch in the inset on the right of (b) shows where defects are introduced, at nearly the same depth of ≈10 ML in one part of each sample. The arrows in (a) indicate  $T_N$  for each sample. For  $x = 0$  and  $x = 50$  we can give only lower limits for  $T_N$ ; this is indicated by horizontal lines connected to the respective arrows. The inset in (a) shows exemplarily with a zoom-in on the data of the non-sputtered sample with  $x = 15$  the procedure of obtaining  $T_N$ . The arrows in (b) indicate  $T_b$ , the inset on the left in (b) explains for the sputtered sample with  $x = 50$  how  $T_b$  was determined. Dotted (solid) arrows represent sputtered (non-sputtered) samples.

larger effect on  $H_c(T)$ . In Figure 7b, it is seen that sputtering at a larger depth is also having a larger effect on the EB. The main effect is not so much to increase the EB field at the lowest temperatures, but to shift up  $T_b$ . As for  $H_c(T)$ ,  $H_{eb}(T)$  for the non-sputtered parts of all samples is about identical, as it should, and confirms the reproducibility of our samples. The Néel temperatures of the samples in Figure 7 are around the upper end of the measured temperature range or higher, such that we can give only a lower limit. The values for  $T_b$  and  $T_N$  for all samples are shown in **Table 1**.

Note that the thickness of the FM Co layer is 5 ML in Figure 6 and 10 ML in Figure 7. The sample with the pure Mn layer in Figure 6 (black data points) and the sample sputtered after the

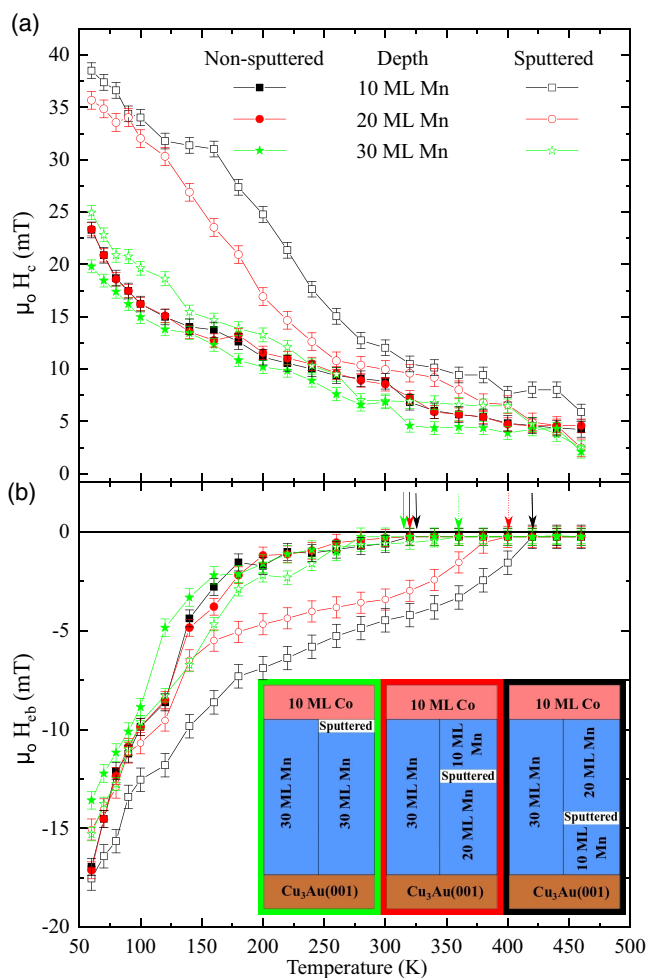


**Figure 7.** a,b) Temperature dependence of  $H_c$  (a) and  $H_{cb}$  (b) for 10 ML Co/30 ML Mn bilayers for both parts (sputtered and nonsputtered) of the samples on  $\text{Cu}_3\text{Au}(001)$ . The inset (sketch) in (b) shows how defects are inserted at different depths in one part of the samples. The frame color of each box in the inset corresponds to the respectively-colored data points in the main figure. The filled symbols are for the nonsputtered parts and the open symbols for the sputtered parts of the samples. The arrows in (b) indicate  $T_b$ , determined in the same way as in Figure 6.

deposition of 10 ML Mn in Figure 7 (also black data points) thus differ only by the thickness of the Co FM layer. If  $H_c$  and  $H_{cb}$  were exclusively determined by the coupling of the FM layer at the interface to the AFM layer, they would depend inversely on the thickness of the FM layer. Comparing the data of these two samples in Figure 6 and 7, one can see that this is about the case, although there are subtle differences.

### 3. Discussion

It is meanwhile established that EB requires uncompensated pinned magnetic moments within the AFM layer that exist due to structural or chemical disorder in the system.<sup>[11,31,32,38,41]</sup> These disorders or defects exist either at the AFM/FM interface

**Table 1.** Néel temperature  $T_N$  and blocking temperature  $T_b$  for all samples for the nonsputtered part and the sputtered part, where defects have been introduced after the listed height of deposition of the AFM layer.

Sample	Sputtered	$T_N$ [K]	$T_b$ [K]
5 ML Co/30 ML $\text{Ni}_{50}\text{Mn}_{50}$	No	$\geq 400$	$140 \pm 10$
	After 10 ML	$\geq 400$	$260 \pm 10$
5 ML Co/30 ML $\text{Ni}_{35}\text{Mn}_{65}$	No	$300 \pm 10$	$240 \pm 10$
	After 9 ML	$300 \pm 10$	$260 \pm 10$
5 ML Co/30 ML $\text{Ni}_{25}\text{Mn}_{75}$	No	$320 \pm 10$	$300 \pm 10$
	After 10 ML	$320 \pm 10$	$320 \pm 10$
5 ML Co/30 ML $\text{Ni}_{15}\text{Mn}_{85}$	No	$320 \pm 10$	$320 \pm 10$
	After 8 ML	$360 \pm 20$	$360 \pm 20$
5 ML Co/30 ML Mn	No	$\geq 400$	$320 \pm 10$
	After 10 ML	$\geq 400$	$420 \pm 20$
10 ML Co/30 ML Mn	No	$\geq 420$	$320 \pm 10$
	After 10 ML	$\geq 420$	$420 \pm 10$
10 ML Co/30 ML Mn	No	$\geq 420$	$320 \pm 10$
	After 20 ML	$\geq 420$	$400 \pm 10$
10 ML Co/30 ML Mn	No	$\geq 420$	$320 \pm 10$
	After 30 ML	$\geq 420$	$360 \pm 10$

or within the bulk of the AFM layer.<sup>[11,31,32,38,41]</sup> Following the idea of the domain-state model,<sup>[6,7,29]</sup> in our previous work, we proposed a model based on a random distribution of pinning centers within the entire AFM layer, caused either by disorder in the  $\text{Ni}_x\text{Mn}_{100-x}$  alloy or local differences in the concentration of Ni and Mn.<sup>[33,38]</sup> These pinning centers interact with the FM layer by a path of direct exchange coupling within the AFM material. The magnetic moment of such a pinning center may in principle point in any direction, depending on the sign and directionality of the coupling to the FM layer, and is set during the field-cooling process. The size of the EB effect is then determined by the number of pinning centers as a function of temperature, weighted by the strength of their coupling to the FM layer. The latter will depend also on the distance of the pinning center to the FM/AFM interface and the properties of the interface. With the experimental results presented here, we analyze the influence of these parameters separately.

We discuss three kinds of defects in our sample that can act as a source of uncompensated pinned moments in the AFM layer. These are: 1) structural defects that occur naturally upon growth of the film, 2) chemical defects upon alloying of Mn and Ni into a chemically disordered  $\text{Ni}_x\text{Mn}_{100-x}$  alloy, and 3) the deliberately introduced structural defects by  $\text{Ar}^+$  sputtering. We discuss their contributions toward the EB effect separately.

Naturally occurring structural defects are unavoidable in all samples and, judged from the relative change in EB due to sputter-defecting or alloying Mn with Ni, are the primary source of uncompensated pinned moments within the AFM layer and hence the EB effect. The chemical defects in the NiMn alloy also play a significant role. In the studied concentration range of  $0 \leq x \leq 50$ , the EB in the nonsputtered samples is smaller at

both extremes, i.e., in pure Mn and in  $\text{Ni}_{50}\text{Mn}_{50}$ , compared with the concentrations in between, see Figure 6. This allows for an estimation of the role of chemical effects by reasoning that for  $x = 50$  the films are more regularly ordered and consequently have less chemical defects. AFM layers with  $x = 0$  and  $x = 50$  exhibit the highest coercivity and, at the same time, the lowest EB field, as seen from the results in Figure 6. This shows that coercive and EB fields are not related in a simple way to each other. The coercivity depends on the coupling at the FM–AFM interface, the amount of reversing unpinned moments in the AFM, and the energy barrier for their reversal. Together, these properties obviously lead to an increase in the coercivity when going away from the Ni concentrations  $x = 0$  and  $x = 50$  to the presumably chemically more disordered alloys with  $x$  in between. An increase in  $H_c(T)$  and  $T_b$  when reducing  $x$  from 50 to 20 has been reported by us previously<sup>[21]</sup> and has been attributed to an increasing magnetic anisotropy and a smaller domain wall width of the AFM layer, leading to a smaller thickness required to establish EB at a fixed temperature.

The deliberately introduced defects enhance both the coercivity as well as the EB field  $H_{eb}$  for all alloy compositions. The enhancement of the EB field corresponds to an increase in the blocking temperature  $T_b$ . The process of sputtering obviously effectively increases the number of pinned moments and thus the EB.

This is again an indication that before sputtering there is a lower number of chemical defects in these samples, such that the relative influence of the sputter-introduced defects on the EB is larger. A higher number of pinning centers that couple to the FM layer enhances the strength of the overall unidirectional coupling and thus results in a higher blocking temperature  $T_b$ . The enhancement of the coercivity paralleling this effect shows that with an increased number of pinning centers there are also competing coupling paths in the AFM that lead to energy dissipation during the reversal of the FM-layer magnetization.

The contribution of the deliberately introduced defects increases with their distance from the FM layer (Figure 7). Defects created at the FM–AFM interface (green symbols in Figure 7) seem to contribute very little to EB, whereas the strongest effect is observed for defects with the largest distance from the interface (black symbols). The small effect of interfacial defects is in line with the domain-state model of EB<sup>[6,7,29]</sup> and experiments proving that the AFM bulk is mainly responsible for EB.<sup>[11,30–34]</sup> As also the coercivity is only weakly affected by the sputtering at the interface, we can assume that the coupling across the interface is not significantly influenced by the sputtering. The stronger effect of the more deeply buried defects is explained by a model we have previously used to explain the increase in  $H_{eb}$  and  $T_b$  with  $\text{Ni}_x\text{Mn}_{100-x}$  AFM layer thickness.<sup>[38]</sup> In a thinner AFM layer, there are fewer pinning centers, but with on average shorter and consequently stronger exchange paths. Stronger coupling between a pinning center and the FM layer results in a higher torque on the pinned moment upon FM-layer magnetization reversal, which lowers the threshold for thermal unpinning. In other words, if a pinning center is too close to the FM layer, no spin spiral or local horizontal domain wall might be accommodated, which would lead either to domains in the FM layer<sup>[5]</sup> or to the unpinning of the uncompensated moments with an enhancement of  $H_c$ . Following that idea, a certain distance is

required for pinning centers to effectively pin the FM-layer magnetization. The results of Figure 7 thus clearly differentiate the contribution of the bulk AFM spin structure from the FM–AFM interfacial contribution. The fact that the AFM bulk spin structure dominantly contributes to the phenomenon of EB is fairly observed here. This very much supports, or rather verifies, the domain-state model for EB. What we cannot exclude, though, is the possibility that the sputtering affects the subsequent growth of the Mn layer and that such a lower position of sputtering leads also to more defects in higher-lying layers.

The relative increase in  $H_{eb}$  upon sputter-defecting the AFM layer is larger at temperatures between about 200 and 300 K compared with the lowest temperatures in the experiment (Figure 7b). This is an indication of two different types of pinning mechanisms dominating the EB at the different temperatures. Between about 200 K and the blocking temperature, the effect of the sputtering is most pronounced. The artificially introduced pinning centers are obviously active at these temperatures, while pinning from the naturally occurring defects does not play a significant role here. The latter lead to a strong increase in the EB only at lower temperatures, below about 150 K, as seen from the undefected samples (filled symbols in Figure 7b). At these temperatures, the relative contribution of the additional defects created by the sputtering of the AFM layer is then smaller. It is also conceivable that the sputtering makes some of the already existing pinning centers thermally more stable, for example by introducing additional close-by defects that locally modify the spin structure, leading to more rigidly pinned pinning sites.

Despite the relatively small ion doses, some removal of material, below the detection limit of AES, is unavoidable in the sputtering process used to introduce the defects. A lower thickness of the AFM layer would lead to a lower value of  $T_b$  and a smaller EB at fixed temperature. As the opposite is observed, the effect of removing AFM material can be neglected in the aforementioned discussion.

## 4. Conclusion

We have show from experimental results obtained by MOKE measurements on epitaxially grown  $\text{Co}/\text{Ni}_x\text{Mn}_{100-x}/\text{Cu}_3\text{Au}(001)$  samples exhibiting EB ( $0 \leq x \leq 50$ ), where in one part of the sample the  $\text{Ni}_x\text{Mn}_{100-x}$  layer is sputtered with a small dose of Ar ions at its surface or at different depths, that structural defects in the AFM layer introduced as a consequence of this sputtering lead to a higher EB field and larger coercivity. We attribute this to a larger amount of magnetic pinning centers in the AFM layer, which are unanimously considered to be the origin of EB. These pinning centers are linked to structural or chemical defects and lead to an increase in the blocking temperature and a concomitant increase in the EB field. This is most pronounced for samples with Ni concentrations of  $x = 0$  and  $x = 50$ , which in the nonsputtered state exhibit a smaller EB effect than the ones with Ni concentrations in between. This can be discussed as the effect of the introduced defects acting as pinning sites for EB, which in addition to the already-present defects determine the strength of the unidirectional anisotropy. Their smaller relative contribution in films with intermediate

Ni concentrations can be attributed to the higher density of chemical defects in the chemically disordered alloy.

Introducing defects in Co/Mn/Cu<sub>3</sub>Au(001) samples, i.e., for  $x = 0$ , at different depths in the AFM Mn layer reveals a stronger effect on the EB for more deeply buried defects, whereas defecting the FM–AFM interface has a minor effect on the magnetic properties of the sample. This, on the one hand, confirms an assumption of the domain-state model of EB, namely that the pinning centers lying within the volume of the AFM layer are contributing the most to the EB effect and not the interfacial ones, on the other hand, it demonstrates a distance dependence of the location of defects from the interface. The latter can be explained by a minimum distance required for an effective twisting of the coupling chain between pinning centers in the AFM layer and the FM-layer magnetization required to observe EB.

With the presented experiments, we have tested the two main ingredients responsible for the EB effect, i.e., the presence of uncompensated pinned magnetic moments acting as pinning centers and the location of these pinning centers within the volume of the AFM layer. We could show that by introducing structural defects in the AFM layer at a certain distance from the interface to the FM layer, both the EB field at a given temperature as well as the blocking temperature for EB can be significantly enhanced. The behavior of the EB upon introducing extra defects by slight sputtering is compatible with a model in which local uncompensated pinned magnetic moments in the AFM layer interact with the FM layer by a path of direct exchange coupling within the AFM material.

## 5. Experimental Section

All measurements were carried out under ultrahigh vacuum conditions with a base pressure of  $2 \times 10^{-10}$  mbar. The Cu<sub>3</sub>Au(100) single crystal with miscut  $\leq 0.1^\circ$  was cleaned by 1.5 keV Ar ion sputtering. After cleaning, the substrate was annealed at 820 K for 5 min and then at 800 K for 30 min to get a smooth and well-ordered surface. The films were grown on the clean substrate by electron-beam-assisted thermal evaporation. Co and Ni were deposited from high-purity rods (Co and Ni: 99.99%), whereas Mn was evaporated from a tantalum crucible filled with pure Mn flakes (99.99%) by electron bombardment with the substrate held at room temperature. The electron beam was focused on the tip of a rod of 2 mm diameter or on the top of the crucible of 6 mm diameter, respectively, which was set to positive high voltage and held in a water-cooled system. The Ni<sub>x</sub>Mn<sub>100-x</sub> films were prepared by simultaneous evaporation of Ni and Mn. The Ni concentration  $x$  was varied by tuning the individual deposition rates. The growth rates of the films are typically from 0.5 to 2 ML per minute, and were checked by counting the oscillations in the (0,0)-spot MEED intensity recorded during evaporation. To create defects inside the AFM layer, we stopped the deposition shortly to expose the surface for 40 s to Ar ions of 1 keV energy, using an Ar pressure of  $2 \times 10^{-5}$  mbar. These exposure conditions were optimized in a way not to lose any measurable part of a monolayer, as detected by Auger electron spectroscopy (AES). By placing a mechanical shutter in front of the substrate, this could be applied to one half of the sample, whereas the other was unaffected.

The  $c(2 \times 2)$  structure, which indicates the ordered arrangement of Cu and Au atoms, was confirmed by low-energy electron diffraction (LEED). MEED is used to monitor the growth of the films and to determine their growth mode. In this study, we used AES in parallel with MEED to determine the thickness of the samples. AES was also used to confirm the cleanliness of the substrate, the Ni concentration in the Ni<sub>x</sub>Mn<sub>100-x</sub> alloy films, and to compare the sputtered and the nonsputtered parts of the sample, to be sure that the thickness of the film did not change. LEED

and LEED I(V) curves are used for analyzing the structure of the prepared films and measuring their perpendicular lattice constants, respectively.

The morphology of RT-grown Mn films was characterized by RT scanning tunneling microscopy (STM) in a separate chamber in which we have grown pure Mn films using the same evaporation parameters. The magnetic properties are finally measured by in situ longitudinal MOKE. Linearly polarized laser light from a laser diode of 1 mW power and 635 nm wavelength was used.

## Acknowledgements

T.S. is grateful for financial support during his stay in Berlin by the Senator of District Khyber (Ex-FATA), Pakistan and Freie Universität Berlin. M.Y.K., I, and M.S. are grateful for financial support during their stay in Berlin by DAAD (Deutscher Akademischer Austauschdienst) (German Academic Exchange Service) through grant nos. 57068383 and 57243485. The authors thank Uwe Lipowski for technical assistance.

Open access funding enabled and organized by Projekt DEAL.

## Conflict of Interest

The authors declare no conflict of interest.

## Data Availability Statement

The data that support the findings of this study are available from the corresponding authors upon reasonable request.

## Keywords

antiferromagnets, epitaxial thin films, exchange bias, NiMn

Received: April 9, 2021

Revised: June 7, 2021

Published online: July 14, 2021

- [1] Y. Wang, C. Song, G. Wang, J. Miao, F. Zeng, F. Pan, *Adv. Funct. Mater.* **2014**, *24*, 6806.
- [2] V. Baltz, A. Manchon, M. Tsoi, T. Moriyama, T. Ono, Y. Tserkovnyak, *Rev. Mod. Phys.* **2018**, *90*, 015005.
- [3] C. Chappert, A. Fert, F. N. Van Dau, in *Nanoscience And Technology: A Collection of Reviews from Nature Journals*, World Scientific, Singapore **2010**, pp. 147–157.
- [4] S. A. Wolf, D. D. Awschalom, R. A. Buhrman, J. M. Daughton, S. von Molnár, M. L. Roukes, A. Y. Chtchelkanova, D. M. Treger, *Science* **2001**, *294*, 1488.
- [5] W. Kuch, F. Offi, L. Chelaru, M. Kotsugi, K. Fukumoto, J. Kirschner, *Phys. Rev. B* **2002**, *65*, 140408.
- [6] P. Miltényi, M. Gierlings, J. Keller, B. Beschoten, G. Güntherodt, U. Nowak, K. D. Usadel, *Phys. Rev. Lett.* **2000**, *84*, 4224.
- [7] U. Nowak, K. D. Usadel, J. Keller, P. Miltényi, B. Beschoten, G. Güntherodt, *Phys. Rev. B* **2002**, *66*, 014430.
- [8] M. Ali, P. Adie, C. H. Marrows, D. Greig, B. J. Hickey, R. L. Stamps, *Nat. Mater.* **2007**, *6*, 70.
- [9] M. G. Blamire, M. Ali, C. W. Leung, C. H. Marrows, B. J. Hickey, *Phys. Rev. Lett.* **2007**, *98*, 217202.
- [10] S. K. Mishra, F. Radu, H. A. Dürr, W. Eberhardt, *Phys. Rev. Lett.* **2009**, *102*, 177208.
- [11] R. Morales, Z. P. Li, J. Olamit, K. Liu, I. K. Alameda, J. M. Schuller, *Phys. Rev. Lett.* **2009**, *102*, 097201.



- [12] F. Radu, H. Zabel, in *Magnetic Heterostructures*, Springer, Berlin, Germany **2008**, pp. 97–184.
- [13] B. Dieny, V. S. Speriosu, S. S. P. Parkin, B. A. Gurney, D. R. Wilhoit, D. Mauri, *Phys. Rev. B* **1991**, *43*, 1297.
- [14] F. Offi, W. Kuch, J. Kirschner, *Phys. Rev. B* **2002**, *66*, 064419.
- [15] W. Kuch, L. I. Chelaru, F. Offi, J. Wang, M. Kotsugi, J. Kirschner, *Phys. Rev. Lett.* **2004**, *92*, 017201.
- [16] M. Y. Khan, C. B. Wu, M. Erkovan, W. Kuch, *J. Appl. Physics* **2013**, *113*, 023913.
- [17] W. A. A. Macedo, P. L. Gastelois, M. D. Martins, W. Kuch, J. Miguel, M. Y. Khan, *Phys. Rev. B* **2010**, *82*, 134423.
- [18] M. Stampe, P. Stoll, T. Homborg, K. Lenz, W. Kuch, *Phys. Rev. B* **2010**, *81*, 104420.
- [19] W. Kuch, L. I. Chelaru, F. Offi, J. Wang, M. Kotsugi, J. Kirschner, *Nat. Mater.* **2006**, *5*, 128.
- [20] C. Tieg, W. Kuch, S. G. Wang, J. Kirschner, *Phys. Rev. B* **2006**, *74*, 094420.
- [21] M. Y. Khan, C. B. Wu, S. K. Kreft, W. Kuch, *J. Phys.: Condens. Matter* **2013**, *25*, 386005.
- [22] M. Y. Khan, *Ph.D. thesis*, Freie Universität Berlin, **2012**.
- [23] C. P. Bean, in *Structure and Properties of Thin Films: Proceedings*, Wiley, New York **1959**, p. 331.
- [24] W. H. Meiklejohn, C. P. Bean, *Physical Rev.* **1956**, *102*, 1413.
- [25] H. Ohldag, A. Scholl, F. Nolting, E. Arenholz, S. Maat, A. T. Young, M. Carey, J. Stöhr, *Phys. Rev. Lett.* **2003**, *91*, 017203.
- [26] D. Mauri, H. C. Siegmann, P. S. Bagus, E. Kay, *J. Appl. Phys.* **1987**, *62*, 3047.
- [27] A. P. Malozemoff, *Phys. Rev. B* **1987**, *35*, 3679.
- [28] R. L. Stamps, *J. Phys. D: Appl. Phys.* **2000**, *33*, R247.
- [29] J. Keller, P. Miltényi, B. Beschoten, G. Güntherodt, U. Nowak, K. D. Usadel, *Phys. Rev. B* **2002**, *66*, 014431.
- [30] Z. Jiao, Q. Qu, Z. Ding, Y. Wang, L. Wu, Y. Zhou, J. Li, *Thin Solid Films* **2020**, *706*, 138008.
- [31] A. C. Basaran, T. Saerbeck, J. Venta, H. Huckfeldt, A. Ehresmann, I. K. Schuller, *Appl. Phys. Lett.* **2014**, *105*, 072403.
- [32] I. K. Schuller, R. Morales, X. Batlle, U. Nowak, G. Güntherodt, *J. Magn. Magn. Mater.* **2016**, *416*, 2.
- [33] M. Y. Khan, Y. A. Shokr, W. Kuch, *J. Phys.: Condens. Matter* **2019**, *32*, 075801.
- [34] A. V. Svalov, G. V. Kurlyandskaya, V. N. Lepalovskij, P. A. Savin, V. O. Vas'kovskiy, *Superlattices Microstruct.* **2015**, *83*, 216.
- [35] M. Reinhardt, J. Seifert, M. Busch, H. Winter, *Phys. Rev. B* **2010**, *81*, 134433.
- [36] Y. A. Shokr, M. Erkovan, C. B. Wu, B. Zhang, O. Sandig, W. Kuch, *J. Appl. Phys.* **2015**, *117*, 175302.
- [37] M. Erkovan, Y. A. Shokr, D. Schiestl, C. B. Wu, W. Kuch, *J. Magn. Magn. Mater.* **2015**, *373*, 151.
- [38] M. Y. Khan, C. B. Wu, W. Kuch, *Phys. Rev. B* **2014**, *89*, 094427.
- [39] K. Lenz, S. Zander, W. Kuch, *Phys. Rev. Lett.* **2007**, *98*, 237201.
- [40] C. Mitsumata, A. Sakuma, K. Fukamichi, *Phys. Rev. B* **2003**, *68*, 014437.
- [41] X. Chi, F. Ma, A. Luo, A. Du, J. Wang, Y. Hu, *Phys. Lett. A* **2015**, *379*, 2772.